Diagnostics of inhomogeneous stellar jets

Convolution effects and data reconstruction

F. De Colle¹, C. del Burgo¹ & A. C. Raga²

- Dublin Institute for Advanced Studies (DIAS), 31 Fitzwilliam Place, Dublin 2, Ireland e-mail: fdc, cburgo@cp.dias.ie
- Instituto de Ciencias Nucleares, Universidad Nacional Autónoma de México, Ap.P. 70543, 04510 DF, Mexico e-mail: raga@nucleares.unam.mx

Preprint online version: October 24, 2018

ABSTRACT

Context. In the interpretation of stellar jet observations, the physical parameters are usually determined from emission line ratios, obtained from spectroscopic observations or using the information contained in narrow band images. The basic hypothesis in the interpretation of the observations is that the emitting region is homogeneous along the line of sight. Actually, stellar jets are in general not homogeneous, and therefore line of sight convolution effects may lead to the main uncertainty in the determination of the physical parameters.

Aims. This paper is aimed at showing the systematic errors introduced when assuming an homogeneous medium, and studying the effect of an inhomogeneous medium on plasma diagnostics for the case of a stellar jet. In addition, we explore how to reconstruct the volumetric physical parameters of the jet (i. e., with dependence both across and along the line of sight).

Methods. We use standard techniques to determine the physical parameters, i. e., the electron density, temperature and hydrogen ionisation fraction across the jet, and a multi-Gaussian method to invert the Abel transform and determine the reconstructed physical structure.

Results. When assuming an homogeneous medium the physical parameters, integrated along the line of sight, do not represent the average of the true values, and do not have a clear physical interpretation. We show that when some information is available on the emissivity profile across the jet, it is then possible to obtain appropriate derivations of the electron density, temperature and ionisation fraction

Key words. ISM: Herbig-Haro objects – ISM: jets and outflows – Techniques: image processing – Methods: data analysis – Stars: pre-main sequence – winds, outflows

1. Introduction

Stellar outflows are generally observed as chains of bright knots with a characteristic spectrum that mainly includes forbidden emission lines (see, e. g., the review by Reipurth & Bally 2001).

Different approaches are used to extract the information on the outflow excitation conditions from the observed emission lines. To calculate the electron density $n_{\rm e}$ the standard method involves the line ratio [SII] $\lambda 6716/\lambda 6731$, which is strongly dependent on n_e and less sensitive to the electron temperature T (see, e. g. Osterbrock 1989). The [SII] ratio, together with the ratios between lines with different excitation temperatures (e. g. $[OI]\lambda 5577/\lambda 6300$) is used to determine both n_e and T. Moreover, the [SII], $[OI]\lambda\lambda6300,6363$ and $[NII]\lambda\lambda6548,6583$ emission lines are often used to calculate, apart from n_e and T, the hydrogen ionisation fraction x_H and the total density $n_{\rm H}$ (= $n_{\rm e}/x_{\rm H}$) (Bacciotti & Eislöffel 1999, hereafter BE99). Additionally, several line ratios in the optical and near infrared wavelength range (e. g. Brugel et al. 1981; Pesenti et al. 2003; Nisini et al. 2005; Podio et al. 2006) can be combined, with weights representing their respective errors (Hartigan & Morse 2007, hereafter HM07), to determine the physical parameters of the HH objects.

Another possibility consists of obtaining predictions of emission line intensities from plane parallel shock models (e. g. Hartigan et al. 1987, Hartigan et al. 1994, Lavalley-Fouquet et al. 2000, Pesenti et al. 2003) or from numerical simulations that include a detailed treatment of the ionisation and recombination evolution of several different species (e. g. Raga 2007), and compare the results with observations.

It is important to develop strategies to properly extract the maximum possible amount of information from the observed line ratios. Convolution, instrumental and observing conditions (i. e. seeing) affect the derivation of physical parameters from observations. Projection or convolution effects are an obvious consequence of the lack of information on the spatial distribution along the line of sight. Additionally, if the cooling region is not resolved the observed emission lines come from regions with different excitation conditions *along* the main jet axis. Actually, also in observations where the cooling region is well resolved the determined parameters are a convolution of the volumetric parameters along the line of sight, i. e. *across* the jet.

Only for an homogeneous medium the mean values of n_e , T, $x_{\rm H}$ (integrated within the beam size and along the line of sight) will coincide with the corresponding values calculated from the observed line ratios. In the case of an inhomogeneous medium

it is necessary to understand what relation holds between the derived and the volumetric mean physical parameters.

This problem has been studied in detail in the context of stellar atmospheres by several authors (e. g. Doschek 1984, Almleaky et al. 1989, hereafter ABS89, Brown et al. 1991, Judge et al. 1997, McIntosh et al. 1998, Judge 2000). As they show the information contained in a set of line ratios may be used to determine the function $\zeta(n_e)$, defined as the "emission measure differential in density", given by $n_e^2(z)dz = \zeta(n_e)dn_e$ (e. g. Judge 2000), where z is the position across the stellar atmosphere. If several line ratios are available, and if the geometry of the system is known, it becomes possible to infer the dependence of the density n_e along the line of sight.

Despite its importance, this problem has not been studied in similar detail in the context of stellar outflows. As far as we are aware, only Safier (1992) studied the influence of inhomogeneities on the density diagnostics in outflows from T Tauri stars, applying a simple model of an isothermal medium with a power law radial dependence for the electron and total densities, and showing that different ratios may be used to obtain information on the density structure.

Recently, observations with information on emission profiles across the jet have been presented by several authors (e. g. Beck et al. 2007, Bacciotti et al. 2000, HM07, Coffey et al. 2007). If the emission line profiles are limited to a few observational values across the jet we will show that this information can be used to derive the values of the physical parameters $n_{\rm e}$, T, and $x_{\rm H}$ assuming a Gaussian profile for the emission lines. If the emission profiles across the jet are well sampled, we will show in this paper how standard tomographic techniques (e. g. Craig & Brown 1986, Brown 1995) may be applied to reconstruct the volume emission line intensities (i. e., the emission coefficients) from the values integrated along lines of sight, which can then be used to determine the $n_{\rm e}$, T and $x_{\rm H}$ cross sections of the jet.

The paper is organised as follows. In Section 2, the effect of stratification on the interpretation of the electron density, temperature and hydrogen ionisation diagnostics is discussed. Section 3 presents a simple technique for obtaining information on the radial structure of the jet, and an example of its application to data of the HH30 jet. Finally, Section 4 summarises the obtained results.

2. Convolution effects on jets

2.1. Convolution effects for a non-resolved jet cross section

We consider an axisymmetric jet in a three - dimensional cartesian reference frame. The *z*-axis of this system is taken along with the main axis of the jet. The observer is looking at the jet along the *y*-axis, and the *xz*-plane coincides with the plane of the sky (see Fig. 1). The cylindrical radius *r* is the distance between an arbitrary point and the *z*-axis.

The jet is observed in the $[SII]\lambda\lambda6716, 6731$, $[OI]\lambda\lambda6300, 6363$ and $[NII]\lambda\lambda6548, 6583$ emission lines. These lines give three ratios which depend on the three variables to be determined: n_e , T, x_H . These emission line intensities are observed at a certain number of points x_i (corresponding to the pixel size) in the plane of the sky.

In the following, capital letters will be used to design quantities integrated and convolved (according to the nature of the variable) along the line of sight, and lower case letters for volume quantities. For instance, i represents the volume emissivity (defined by eq. A.1), while I is the intensity (i. e. the emissivity *integrated* along the line of sight, with units: erg s⁻¹ cm⁻² sr⁻¹);

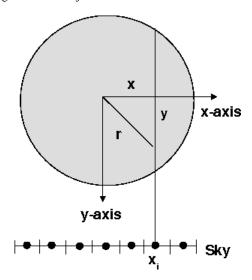


Fig. 1. Schematic representation of a cross section of a stellar jet. The jet is moving in the direction perpendicular to the plane of the image (the z-axis, not shown in the Figure), and is assumed to be axisymmetric. The observer is looking at the jet along the y-direction, and the observations are represented by a series of points along the x-axis, each one corresponding to the pixel size and obtained integrating the volume intensities along the line of sight and on the beaming size $\Delta x \Delta z$.

 $n_{\rm e}$ represents the electron density across the jet, while $N_{\rm e}$ is the electron density obtained *convolving* $n_{\rm e}$ on a volume element. Only the electron temperature is designed by T in both cases.

To clarify the effect of inhomogeneities on plasma diagnostics, first some results from ABS89 are reviewed. The ratio G_{12} between two observed line luminosities is given by:

$$G_{12} = \frac{\int i_1 dV}{\int i_2 dV},\tag{1}$$

where dV is the volume element. Volume and integrated ratios have the same value if the medium is homogeneous.

In general the line ratios also depend on T and $x_{\rm H}$, but the following analysis is focused on ratios between lines emitted from the same species (independent of $x_{\rm H}$) and nearly independent of T (e. g. the red [SII] ratio). Assuming a medium with a uniform electron density $n_{\rm e,0}$, eq. 1 leads to $G_{12}=i_1/i_2=g_{12}(n_{\rm e,0})$. Inverting this equation it is possible to determine the density as $n_{\rm e,0}=g_{12}^{-1}(G_{12})$.

If the medium is inhomogeneous, the previous formula may also be applied to give a "spectroscopic electron mean density" defined as (ABS89):

$$< n_{\rm e} > = g_{12}^{-1} \left[\frac{\int i_1 dV}{\int i_2 dV} \right].$$
 (2)

The volume emissivities for the line j may be written as (e. g. ABS89, Osterbrock 1989, Safier 1992):

$$i_j = k_j \frac{n_e^2}{1 + n_e/n_j},$$
(3)

This expression is exact for a two-level atom. In this case, $n_j = A_{2,1}/(C_{2,1} + C_{1,2})$ is the "critical density" and $k_j = \frac{1}{4\pi}h\nu_{2,1}(C_{1,2}/x_{\rm H})(n_{\rm s}/n_{\rm H})$, where $A_{2,1}$ is the Einstein-A coefficient for the transition, $C_{1,2}$ and $C_{2,1}$ are the collisional excitation and de-excitation rates respectively, $h\nu_{2,1}$ is the transition energy, and

 $n_{\rm s}/n_{\rm H}$ is the population fraction of the species s. A fit with eq. 3 is also a very good approximation for many forbidden emission lines, in particular for the red [SII] lines.

Using eq. 3 for replacing i_i in eq. 1, we then have:

$$\langle n_{\rm e} \rangle = \frac{k_1/k_2 - G_{12}}{G_{12}/n_1 - k_1/(k_2 n_2)}.$$
 (4)

This equation is next applied to the case of a stellar jet (see Fig. 1), first considering spectroscopic observations with a long slit along the jet axis, where no spatial information across the jet is available. The observed line emissivity will be given by the integration of the volume emissivity within the jet volume, where $dV = 2\pi r dr \Delta z$, being Δz the size of the beam in the z direction.

If the electron density is represented by a Gaussian radial profile, then $n_e = n_0 e^{-r^2/\sigma^2}$, and the spectroscopic mean density defined by eq. 4 becomes:

$$\langle n_{\rm e} \rangle = \frac{(n_1 - n_2)(n_0 - n_{\rm ex}) - n_1^2 L_1 + n_2^2 L_2}{n_1 L_1 - n_2 L_2},$$
 (5)

where $L_{1,2} = \ln(1 + n_0/n_{1,2})/(1 + n_{\rm ex}/n_{1,2})$, with n_0 the electron density on the jet axis and $n_{\rm ex}$ the density evaluated at the jet radius. This is the same expression derived by ABS89 for the case of an exponentially decreasing density in an isothermal stellar atmosphere.

On the other hand, the mean electron density across the jet is given by:

$$\overline{n}_{\rm e} = \frac{\int n_{\rm e}dV}{\int dV} = \frac{n_0 - n_{\rm ex}}{\log (n_0/n_{\rm ex})},\tag{6}$$

where the right hand side term is obtained as before assuming a Gaussian density profile and $dV = 2\pi r dr \Delta z$.

The ratio between mean spectroscopic density and mean density (i. e. the ratio between the "observed" and the "real" density) is shown in Fig. 2 as a function of the central electron density for the [SII] ratio. Similar curves were calculated by ABS89 for line ratios relevant to stellar atmospheres.

As can be seen from Fig. 2, the ratio between the spectroscopic and the mean density increases for steeper stratifications of $n_{\rm e}$ across the beam of the jet. At a fixed limb-to-centre electron density ratio $n_{\rm ex}/n_0$, the $< n_{\rm e} > /\overline{n}_{\rm e}$ ratio is slowly decreasing. The spectroscopic mean density is always larger than the mean density because denser regions contribute more to the emission. In the low density regime $(n_0, n_{ex} \ll n_j)$ in particular, it is straightforward to show that eq. 5 reduces to $< n_{\rm e} > /\overline{n}_{\rm e} \approx (2/3)(\alpha^2 + \alpha + 1)/(\alpha^2 - 1) \ln \alpha$ where $\alpha = n_0/n_{ex}$, and $< n_{\rm e} > /\overline{n}_{\rm e} \approx 2/3 \ln \alpha$ when $n_0 \gg n_{ex}$ as in the upper curves of Fig. 2.

The results shown in Fig. 2 are particularly relevant for stellar jets because an important parameter that is determined observationally is the mass flux (and the momentum flux, that has the same behaviour, as described below), defined by $d\dot{M} \sim \rho v r dr$, where ρ is the mass density ($\propto n_{\rm H} = n_{\rm e}/x_{\rm H}$) and v(r) is the jet velocity. If velocity and ionization fraction have a "top-hat" profile in the r direction, it may easily be shown that:

$$\frac{\overline{\dot{M}}}{\langle \dot{M} \rangle} = \frac{\overline{n}_{\rm e}}{\langle n_{\rm e} \rangle},\tag{7}$$

where $\overline{\dot{M}}$ is the mass flux and the $\langle \dot{M} \rangle$ is the one determined using the spectroscopic mean density. Therefore, values of mass and momentum-flux represent just an upper limit to the real values (see e. g. Cabrit 2002).

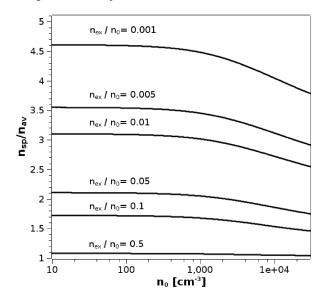


Fig. 2. Ratio between the spectroscopic n_{sp} and average density n_{av} as a function of the density n_0 on the jet axis, for different jet cross sections, characterized by their limb-to-centre electron density ratio $n_{\rm ex}/n_0$.

2.2. Convolution effects for a resolved jet cross section

We now consider the case where information on the emission profile across the jet is available. The volume and integrated emissivities i(r) and I(x) are related to each other by the Abel transform:

$$I(x) = 2 \int_{x}^{R} \frac{i(r)rdr}{\sqrt{r^{2} - x^{2}}},$$
 (8)

where R is the jet radius and x is the projected separation between a point in the observed image and the projection of the jet axis on the plane of the sky.

In the case of an homogeneous medium $i = i_0$ and eq. 8 leads to $I(x) = 2i_0 \sqrt{R^2 - x^2}$. To show the effect of an inhomogeneous medium on plasma diagnostics, in the following we present results obtained numerically integrating eq. 8 for different $n_{\rm e}$, T, $x_{\rm H}$ profiles.

Assuming a profile for n_e , T, x_H , for each radial position the synthetic emissivities in the [SII] $\lambda\lambda6716$, 6731, [NII] $\lambda6583$, and [OI] $\lambda6300$ lines are calculated, solving the statistical equilibrium equations using a 5-level atom (with atomic parameters from Mendoza 1983). These spatially dependent emission coefficients are then used to numerically integrate eq. 8. Finally, the physical parameters are determined from the integrated emission line intensities using the BE method (see Appendix A).

The results obtained assuming a Gaussian profile for n_e , and constant T and x_H cross sections are shown in Fig. 3. The volume and integrated emissivities of [SII] λ 6716 and [SII] λ 6731 versus r/R are shown in the top panel, both normalised to their values at r=0. The [SII] ratio is also shown in the central panel of Fig. 3 while the volume and integrated electron densities are shown in the lower panel.

The [SII] ratio determined using the integrated emissivities is higher than the original ratio (continuous and dotted line of Fig. 3, respectively). The difference between n_e and N_e increases from 0 at the external radii to approximately 20% toward the jet axis.

Fig. 4 shows the ratio n_0/N_0 between the original and convolved values of the electron density on the jet axis versus the

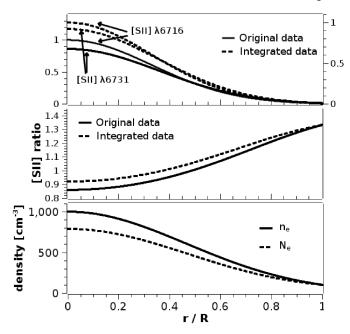


Fig. 3. Effect of the convolution on inhomogeneous jets. The dotted lines represent integrated quantities, while the continuous lines represent volume quantities. The electron density has a Gaussian profile ranging between 10³ cm⁻³ on the axis and 100 cm⁻³ at the jet radius. The temperature and the ionisation fraction are assumed to have constant values of 10⁴ K and 0.1, respectively. Top: [SII] λ 6716, λ 6731 integrated and volume intensities. Centre: $[SII]\lambda 6716/\lambda 6731$ integrated and volume ratio. Bottom: volume and integrated electron density.

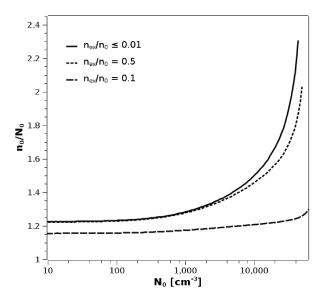


Fig. 4. Ratio between convolved and volumetric densities for different values of $n_0/n_{\rm ex}$.

convolved electron density N_0 , for different values of $n_{\rm ex}/n_0$. As is evident from the figure, the convolution effect increases when the observed density approaches the critical density (of $\sim 10^4 \text{ cm}^{-3}$) for the [SII] ratio. For high density stratifications, the n_0/N_0 ratio converges to a maximum ratio, which depends on the value of N_0 .

Fig. 5 shows the results obtained for different profiles for n_e and top hat cross sections for T and x_H . The differences between n_0 and N_0 goes up to ~ 60% for the most stratified case (bottom

Fig. 6 shows the results obtained for different initial stratifications in n_e , T and x_H , corresponding to radial profiles with the form $\sim 10^{-(r/R)^{\beta}}$ where $\beta = 2, 1, 0.5$ for the top, centre and bottom panels of Fig. 5 and 6 respectively.

It is clear from Fig. 6 that effects similar to the one observed for n_e in Fig. 3 are present also for T and x_H . Additionally, Fig. 5 and 6 show that convolution effects increase with the plasma stratification (as expected).

3. Data reconstruction

3.1. Reconstruction of the jet structure using a Gaussian fit to the observed intensities

The volume emission coefficient projected on the sky plane is also weighted on the beam size $\Delta x \Delta z$. Therefore, the observed emissivity $I(x_i)$ is given by:

$$I(x_i) = 2\Delta z \int_{x_{i+1/2}}^{x_{i+1/2}} dx \int_{x}^{R} \frac{i(r)rdr}{\sqrt{r^2 - x^2}},$$
 (9)

where i = -N, ..., 0, ..., N, there are 2N + 1 observational values (with N = 0, 1, 2, ...), and $i_{\pm (N+1/2)} = R$. All the relevant quantities are assumed to have negligible variations in the z direction.

A simple scaling between i(r) and I(x) may be obtained in the case of an inhomogeneous medium, using the linearity of the Abel transform of a Gaussian distribution. In fact, if the volume emissivity has the form $i(r) = i_0 e^{-r^2/\sigma^2}$, eq. 8 leads to:

$$I(x) = \sqrt{\pi \sigma i(x)} \operatorname{erf} \sqrt{\ln \frac{i_0}{i_{\text{ex}}} \left[1 - \left(\frac{x}{R} \right)^2 \right]}, \tag{10}$$

$$\operatorname{erf}(x) = \frac{2}{\sqrt{\pi}} \int_0^x e^{-t^2} dt \tag{11}$$

is the error function, and i_0 and i_{ex} are the volume emissivity at the jet centre and limb, respectively.

The property of the error function: $erf(x) \approx 1$ when $x \gtrsim 1$ implies that

$$I(x) \approx \sqrt{\pi}\sigma i(x)$$
 (12)

if $x \lesssim R$ and $i_0 \gg i_{ex}$. Using I(x) as given by eq. 12, eq. 9 becomes:

$$I(x_i) = \pi \sigma^2 i_0 \left(\operatorname{erf} \frac{x_{i+1/2}}{\sigma} - \operatorname{erf} \frac{x_{i-1/2}}{\sigma} \right) \Delta z, \tag{13}$$

If only one value of *I* is observed $(x_{i+1/2} = -x_{i-1/2} = R)$, the integrated emissivity will be simply given by:

$$I = \pi \sigma^2 i_0 \left(1 - e^{-R^2/\sigma^2} \right) \Delta z \approx \pi \sigma^2 i_0 \Delta z. \tag{14}$$

Given eq. 14, the relation between the integrated ratio G and the corresponding volume ratio g, in the case of Gaussian profile emissivities, is given by:

$$G = \eta g$$
 where $\eta = \left(\frac{\sigma_1}{\sigma_2}\right)^2$. (15)

If $\sigma_1 \neq \sigma_2$, the integrated and volume ratios will be different. Therefore, the physical parameters determined from the integrated ratio will be different with respect to the one obtained

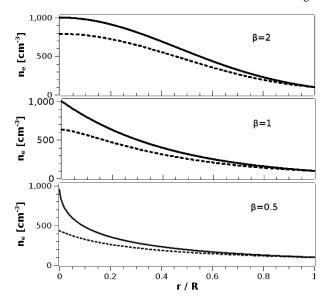


Fig. 5. The dotted lines represent convolved quantities, and the continuous lines represent volume quantities. The curves correspond to the integrated and volume densities, obtained using the following initial profiles: $n \sim 10^{-(r/R)^{\beta}}$, T = 10000 K, $x_{\rm H} = 0.1$ where $\beta = 2, 1, 0.5$ in the upper, central and lower panel respectively. The volume electron density is $1000 \, {\rm cm}^{-3}$ on the axis and $100 \, {\rm cm}^{-3}$ at the jet radius.

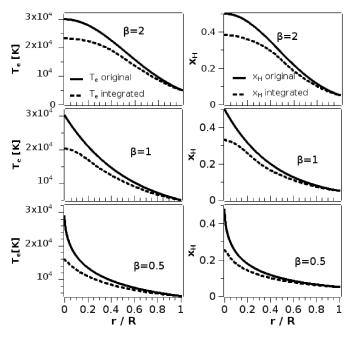


Fig. 6. Effect of the convolution on inhomogeneous jets. The dotted lines represent integrated quantities, and the continuous lines represent volume quantities. Thin lines correspond to the ionisation fraction, and thick lines to the temperature. The curves are obtained using the following profiles: T_e , x, $n_e \sim 10^{-(r/R)^{\beta}}$, where $\beta = 2, 1, 0.5$ in the upper, central and lower panel, respectively.

using the *volume ratio*. Furthermore, the simple scaling given by eq. 15 may be used to reconstruct the volume intensities given the integrated intensities and the values of σ_1 and σ_2 , and from there to determine the radial dependence of the physical parameters.

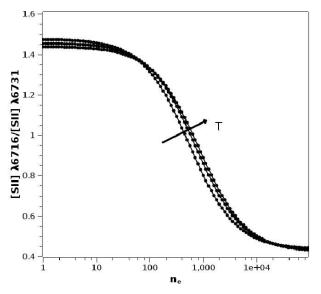


Fig. 7. [SII] λ 6716/ λ 6731 ratio (points) and fits (lines) with eq. 16, corresponding to different temperatures. The fitting parameters are the following: $n_0 = 1841.89$, 2457.4, 2883.9 cm⁻³, $a_1 = 0.678$, 0.687, 0.695, $a_2 = 2.295$, 2.333, 2.336 for T = 5000, 10000, 15000 K, respectively.

We first show how to apply eq. 15 to the [SII] ratio to determine n_e , and later the results will be generalised to more line ratios, to determine all of the physical parameters.

A very good approximation to the relation between the [SII] ratio and n_e may be obtained from eq. 4 and is given by:

$$g = \frac{n_{\rm e} + n_0}{n_{\rm e}a_2 + n_0a_1},\tag{16}$$

where the parameters n_0 , a_1 and a_2 are in general temperature dependent. This formula is exact for a two-level atom, and in general is just a fit to the $g = g(n_e)$ curve at constant T and x_H . Fig. 7 shows the [SII] ratio and the fit calculated using eq. 16. The fitting parameters are reported in the Figure caption as a function of temperature.

In eq. 16, n_e and g represent the volume electron density and ratio respectively. A similar relation will also link the integrated quantities N_e and G:

$$G = \frac{N_{\rm e} + n_0}{N_{\rm e}a_2 + n_0 a_1}. (17)$$

Using eq. 15, 16 and 17 it is possible to obtain a relation between n_e and N_e :

$$n_{\rm e} = n_0 \frac{N_{\rm e}(\eta a_2 - a_1) + n_0 a_1(\eta - 1)}{N_{\rm e} a_2 (1 - \eta) + n_0 (a_2 - \eta a_1)}.$$
 (18)

Fig. 8 shows the ratio between the volumetric and the observed densities $n_{\rm e}/N_{\rm e}$ (obtained from eq. 18) as function of $N_{\rm e}$, for different values of η . For electron densities $N_{\rm e} \gtrsim 5000~{\rm cm}^{-3}$ and $N_{\rm e} \lesssim 100~{\rm cm}^{-3}$, the $n_{\rm e}/N_{\rm e}$ ratio becomes increasingly larger. These density ranges correspond to the high and low-density regimes (see Fig. 7). Also, for densities around $10^3~{\rm cm}^{-3}$, the differences may be as high as a factor of 2 or 3, depending on the value of η .

This procedure may naturally be generalised to include the calculation of T and x_H :

- for each line with spatial information across the jet, the value of σ is obtained with a Gaussian fit to the observed emission profile.

- The volumetric line ratios are reconstructed using eq. 15 as $g_{1,2}=i_1/i_2=\sigma_2/\sigma_1G_{1,2}$.
- The reconstructed ratios are used to determine the physical parameters using any of the available methods (e. g. the BE method, see Appendix A).

If the jet is observed through a narrow slit placed along the main jet axis, eq. 13 has to be used instead of eq. 14. Therefore, η will be defined in this case as:

$$\eta = \left(\frac{\sigma_1}{\sigma_2}\right)^2 \frac{\operatorname{erf}(\Delta x/\sigma_1)}{\operatorname{erf}(\Delta x/\sigma_2)},\tag{19}$$

where Δx is the beam size along the *x*-direction.

3.2. Reconstruction of the jet structure using tomographic techniques

The Abel transform (eq. 8) has been largely studied and applied in science, and complex methods were developed to solve it (e. g. Craig & Brown 1986). The analytical solution of the Abel transform is also well known:

$$i(r) = -\frac{1}{\pi} \int_{r}^{R} \frac{dI}{dx} \frac{dx}{\sqrt{x^{2} - r^{2}}}.$$
 (20)

The determination of i(r) represents an "ill-posed" problem in the sense that small noise in I(x) produces large errors in the determination of i(r), due to the numerical derivative present in the integral. Any numerical method solving eq. 20 using noisy observed data is therefore necessarily unstable.

A method that is less affected by numerical instabilities is obtained by fitting the data by a smooth function and using eq. 20 to invert the fitted curve (e. g. Simonneau 1993). In this context, we use the multi-Gaussian method developed by Bendinelli (1991), which has been mainly used for deprojection of galaxy surface brightness distribution (e. g. Bendinelli 1991, Emsellem et al. 1994, Bendinelli & Parmeggiani 1995, Cappellari 2002). This method basically consists of producing a multi-Gaussian expansion fit of the data, and inverting the Gaussian series. Actually, this approach becomes very simple once the fit has been obtained, due to the already mentioned linearity of the Abel transform when applied to a Gaussian distribution. This implies that for a fit to a data series with a sum of Gaussians (centred on the same point):

$$I(x) = \sum_{i=1}^{n} a_i e^{-x^2/\sigma_i^2},$$
(21)

the Abel transform may be inverted analytically (eq. 20) to give:

$$i(r) = \sum_{i=1}^{n} \frac{1}{\sqrt{\pi}} \frac{a_i}{\sigma_i} e^{-r^2/\sigma_i^2},$$
(22)

where r is the distance from the jet axis.

3.3. Application to HH30

We now apply the techniques derived above to the HH30 jet. HH30 is an ideal candidate for this analysis. It moves nearly on the sky plane, has a clear side-to-side symmetry in the region close to the central star, and the cooling region is resolved spatially with Hubble Space Telescope (HST) observations (e. g. Burrows et al. 1996, Ray et al. 1996, Bacciotti et al. 1999,

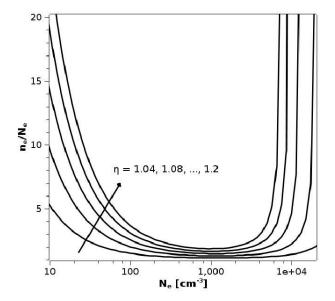


Fig. 8. Ratio of volume and integrated electron densities as a function of the integrated electron density for different values of η .

Table 1. Data fit with Gaussian curves

Gaussian Number	x_0	σ
1	20.97757	153.4
2	20.98055	30.62
3	20.98054	16.42
4	20.98061	15.71
5	20.98061	15.69

HM07). The data used for this analysis were taken by HST using the slit-less spectroscopy technique, and presented by HM07. Using this powerful technique, the observations by HM07 resolve the cross section of the HH30 jet with $\sim 10 - 20$ pixels.

One position along the jet axis is considered here, at an angular separation of 3.9" from the HH30 source, corresponding to a region close to the central star-disk system.

First, to calculate the centre x_0 of the Gaussian fit, i. e. the projection of the jet axis on the plane of the sky, all the observed profiles are added. The obtained emissivity is then fitted with an increasing number of Gaussians. The values of x_0 and the variance σ obtained using up to 5 Gaussians are shown in Tab. 1. Fig. 9 shows the data and a fit with 3 Gaussians (top), and the residual (bottom). From Tab. 1 and Fig. 9 it is evident that a very good approximation to the data is obtained already with 3 Gaussians.

The results obtained are shown in Fig. 10 and Fig. 11. Each emissivity profile is fitted with a multi-Gaussian fit, and using eq. 22 the intensities as a function of the radial position, and the corresponding ratios are reconstructed.

Fig. 10 shows the observed data, the multi-Gaussian fit (top) and the reconstructed data (bottom). The ratios calculated using the reconstructed data differ from the original, observed ratios (see for example the [SII] $\lambda 6716$ curves with respect to the [NII] in the upper and lower panels of Fig. 10).

The physical quantities are shown in Fig. 11. In the upper panel n_e is shown. The points correspond to the observed values, while the continuous and dotted lines correspond to the multi-Gaussian fit and the reconstructed electron density values, re-

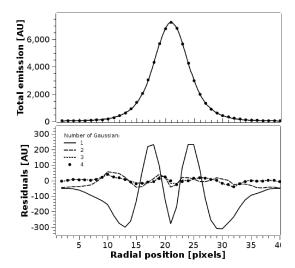


Fig. 9. *Upper panel*: Observed line emissivities (points) and multi-Gaussian fit as a function of the position across the jet using 3 Gaussian curves. *Lower panel*: Residuals for a different number of multi-Gaussian fits.

spectively. The central and lower panels show the temperature and the ionisation fraction.

Some interesting features may be noted from Fig. 11. First at all, it is evident that HH30 does not have a top hat cross section. The reconstructed $n_{\rm e}$, T and $x_{\rm H}$ cross sections are much steeper than the measured cross sections. The reconstructed electron density and ionisation fraction cross sections have strong, on-axis peaks, and the temperature has an on-axis valley. The total densities ($n_{\rm H} = n_{\rm e}/x_{\rm H}$) are larger by a factor of two and four on the jet axis with respect to the jet radius, for the inferred from observation and reconstructed case respectively. The fact that we have lower temperatures in the denser regions is qualitatively consistent with the stronger cooling that one would expect in higher density regions. The fact that the ionisation fraction is higher in the denser regions, however, is an effect that escapes simple qualitative arguments, and should be compared directly with predictions of jet formation and propagation.

It is important to note that the original data were not deconvolved with the PSF (with a width of ≈ 2.5 pixels), and we may expect a much stepper profiles using deconvolved data. Also, the jet presents some degree of asymmetry (see e. g. the wings of the observed temperature in the central panel of Fig. 11). All of these effects, together with a complete study of the two-dimensional structure of the HH30 jet are left for a second paper.

It should be noted that the results shown in Fig. 11 are affected by the fact that the [SII] ratio is close to the high density regime (see Fig. 8). Other line ratios (see the discussion by HM07) should be used to deconvolve the jet beam closed to the source.

4. Summary and discussion

In this paper we have studied the influence of inhomogeneities on the electron density, temperature and ionisation fraction values derived from observed line ratios. Additionally, we have presented possible methods to analyse the data obtained from high angular resolution imaging of stellar jets.

Simple scalings are possible when a minimum amount of information is available. This minimum information is one value of emission line intensities for each position along the jet, to-

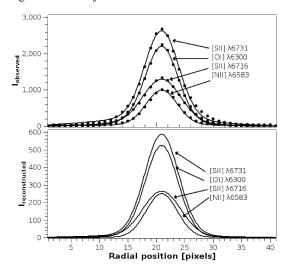


Fig. 10. *Upper panel*: Observed line emissivities (points) against multi-Gaussian fit as a function of the position across the jet. *Lower panel*: Reconstructed line emissivity.

gether with a determination of the jet width σ for *all* of the different lines used for the plasma diagnostics.

Bacciotti et al. (2000) observed DG Tau with 7 narrow slits parallel to the main jet axis, and at different positions across the jet, while Coffey et al. (2007) used one slit placed perpendicular to the main jet axis. In both cases, they obtained spatial and kinematic information across the jet axis. The approach presented in §3.1 can be easily applied to these data, calculating the average physical parameters *and* jet velocity as a function of position along the jet. The determination of the jet velocity has not been explicitly discussed in the present paper, but similar methods to the ones that we have discussed above can be used in this context.

We have also shown that a more complex tomographic reconstruction (see §3.2) can be used to reconstruct the cross section of the flow, obtaining a complete description of the three dimensional structure of the jet.

The main limitations for the application of these techniques is that the jet axis has to lie close to the plane of the sky. However, it would be possible (but more complex) to reconstruct the 3D structure of the flow for arbitrary orientations of the jet axis. Additionally, the jet has to be nearly axisymmetric. Also, the applicability of the present deconvulation method is limited to the nearly axysymmetric region of the jet close to the source. Farther away from the source, in fact, the interaction of the jet with the ambient medium produces asymmetries in the intensity cross-sections.

Finally, while this technique is currently applicable to a few observed objects, the use of future high resolution instruments of the new generation of telescopes will make it possible to apply this technique to a larger sample of objects.

In this paper, preliminary application of our method to reconstructing the cross section of the HH 30 jet has been presented. In a second paper, we will describe a much more complete application of our method using observations of HH 30 and of other HH jets.

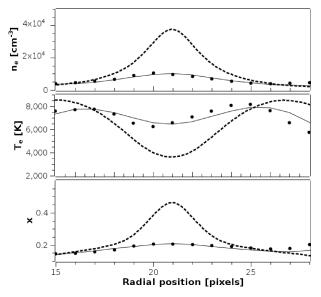


Fig. 11. Values inferred from observations (points), fitted values (with a multi-Gaussian, continuous line) and reconstructed values (dotted line) of electron density, temperature and ionisation fraction for the upper, central and lower panels respectively.

Appendix A: BE method

The emission coefficient (units: erg s⁻¹ cm⁻³ sr⁻¹) obtained by the transition from the i to j levels is given by:

$$i_{i,j} = \frac{1}{4\pi} h v_{i,j} A_{i,j} \frac{n_i}{n_{A_i}} \frac{n_{A_i}}{n_A} \frac{n_A}{n_H} n_H,$$
 (A.1)

where $hv_{i,j}$ is the transition energy, $A_{i,j}$ is the spontaneous Einstein coefficient, n_i/n_{A_i} , n_{A_i}/n_A and n_A/n_H are the excitation fraction, the ionisation fraction and the population fraction of the considered species.

The BE method (from BE99) uses a series of line ratios to determine $n_{\rm e}$, T, $x_{\rm H}$: [SII] λ 6731/[SII] λ 6716, [OI] λ 6300/[SII] λ 6716 + 6731, [NII] λ 6583/[SII] λ 6716 + 6731. The [SII] ratio depends on $n_{\rm e}$ and T, while the [OI]/[SII] and [NII]/[SII] ratios depend also on $n_{\rm OI}/n_{\rm SII}$ and $n_{\rm NII}/n_{\rm SII}$ respectively. Additionally, nitrogen and oxygen ionisation fraction are determined assuming charge exchange equilibrium with hydrogen. Therefore $n_{\rm OI}/n_{\rm SII}$ and $n_{\rm NII}/n_{\rm SII}$ become a function of the ionisation fraction and $n_{\rm O}/n_{\rm S}$ and $n_{\rm N}/n_{\rm S}$ respectively. Finally, the sulphur is supposed to be all single ionised ($n_{\rm SII}$ = $n_{\rm S}$) because the photoionisation rate due to diffuse UV radiation (e.g. Tielens 2005, pp. 267) is much larger than the SII radiative recombination rate.

To calculate the physical quantities, we choose arbitrary values of temperature and ionisation fraction, and invert the [SII] ratio deducing the electron density. Furthermore we use the N/S ratio and the electron density derived previously to determine the ionisation fraction, and finally we use the O/S ratio to find the electron temperature. Finally, we iterate until convergence using the new values of T and $x_{\rm H}$.

The atomic parameters used to calculate collisional ionisation, radiative + dielectronic recombination and charge exchange coefficients are from Cox (1970), Aldrovandi & Péquignot (1973, 1976) and Osterbrock (1989).

Acknowledgements. The authors kindly acknowledge Edith Salado Lopez for the elaboration of Fig. 1, and Linda Podio for useful discussions. A special

thanks to Pat Hartigan for sharing his HH30 data. FDC acknowledges Catherine Dougados for an inspiring lecture on the effects of inhomogeneities on stellar jets during the V Jetset School. FDC also acknowledges support of the European Community's Marie Curie Actions - Human Resource and Mobility within the JETSET (Jet Simulations, Experiments and Theory) network under contract MRTN-CT-2004 005592. AR acknowledges support from the DGAPA (UNAM) grant IN108207, from the CONACyT grants 46828-F and 61547, and from the "Macroproyecto de Tecnologías para la Universidad de la Información y la Computación" (Secretaría de Desarrollo Institucional de la UNAM). Finally, the authors thank the anonymous referee for useful comments.

References

Aldrovandi, S. M. V., & Péquignot, D. 1973, A&A, 25, 137 Aldrovandi, S. M. V., & Péquignot, D. 1976, A&A, 47, 321 Almleaky, Y. M., Brown, J. C., & Sweet, P. A. 1989, A&A, 224, 328 (ABS89) Bacciotti, F., & Eislöffel, J. 1999, A&A, 342, 717 (BE99) Bacciotti, F., & Eislöffel, J., & Ray, T. P 1999, A&A, 350, 917 Bacciotti, F., Mundt, R., Ray, T. P., et al. 2000, ApJ, 537, L49 Beck, T. L., Riera, A., Raga, A. C., et al. 2007, AJ, 133, 1221 Burrows, C. J., Stapelfeldt, K. R., Watson, A. M., et al. 1996, ApJ, 473, 437 Bendinelli, O. 1991, ApJ, 366, 599 Bendinelli, O., & Parmeggiani, G. 1995, AJ, 109, 2 Brown, J. C., Dwivedi, B. N., Sweet, P. A., et al. 1991, A&A, 249, 277 Brown, J. C. 1995, Inverse Problems, 11, 783 Brugel, E. W., Boehm, K. H., & Mannery, E. 1981, ApJS, 47, 117 Cabrit, S., 2002, Constraints on accretion-ejection structures in young stars, ed. J. Bouvier & J.-P. Zahn, EDP Sciences, 3, 147 Cappellari, M. 2002, MNRAS, 333, 400 Coffey, D., Bacciotti, F., & Podio, L. 2007, ApJ submitted Cox, D. P. 1970, Ph.D. Thesis, Univ. of California, San Diego, USA Craig I. J. D., & Brown, J. C., 1986, Inverse problems in astronomy - A guide to inversion strategies for remotely sensed data, Adam Higler, Bristol Doschek, G. A. 1984, ApJ, 279, 452 Emsellem, E., Monnet, G, & Bacon, R. 1994, A&A, 285, 723 Hartigan, P., Raymond, J., & Hartmann, L. 1987, ApJ, 316, 323 Hartigan, P., Morse, J. A., & Raymond, J. 1994, ApJ, 436, 125 Hartigan, P. & Morse, J. 2007, ApJ, 660, 426 (HM07) Judge, P. G. 2000, ApJ, 531, 585 Judge, P. G., Hubeny, V., & Brown, J. C. 1997, ApJ, 475, 275 Lavalley-Fouquet, C., Cabrit, S., & Dougados, C., 2000, A&A, 356, 41 Mendoza, C. 1983, Planetary Nebulae, ed. D. Flower (Reidel), IAU Symp., 103, 143 McIntosh, S. W., et al. 1998, A&A, 333, 333

Nisini, B., Bacciotti, F., Giannini, T., et al. 2005, A&A, 441, 159
Osterbrock, D. E., Astrophysics of gaseous nebulae and active galactic nuclei,
University Science Books (1988)

Pesenti, N., Dougados, C., Cabrit, S., et al. 2003, A&A, 410, 155 Podio, L., Bacciotti, F., Nisini, B., et al. 2006, A&A, 456, 189 Raga, A. C., De Colle, F., Kajdič, P., et al. 2007, A&A, 465, 879 Ray, T. P., Mundt, R., Dyson, J. E., et al. 1996, ApJ, 468, 103 Reipurth, B., & Bally, J. 2001, ARA&A, 39, 403 Safier, P. N. 1992, ApJ, 392, 492

 Simonneau, E., Varela, A. M., Muñoz-Tuñón, C. 1993, JQSRT, 49, 149
 Tielens, A. G. G. M., The Physics and Chemistry of the Interstellar Medium, 2005, Cambridge Univ. Press, Cambridge (UK)